HOKKAIDO UNIVERSITY

Title	Experimental demonstration and mechanism of mitigating reentry blackout via surface catalysis effects
Author(s)	Takasawa, Hideto; Takahashi, Yusuke; Oshima, Nobuyuki et al.
Citation	Journal of Physics D : Applied Physics, 54(22), 225201 https://doi.org/10.1088/1361-6463/abe746
Issue Date	2021-03-08
Doc URL	https://hdl.handle.net/2115/93634
Rights	This is the Accepted Manuscript version of an article accepted for publication in Journal of Physics D : Applied Physics . IOP Publishing Ltd is not responsible for any errors or omissions in this version of the manuscript or any version derived from it. The Version of Record is available online at 10.1088/1361-6463/abe746.
Type	journal article
File Information	J. phys. D 54-22_225201.pdf

Hokkaido University Collection of Scholarly and Academic Papers : HUSCAP

Experimental Demonstration and Mechanism of Mitigating Reentry Blackout via Surface Catalysis Effects

Hideto TAKASAWA[1], Yusuke TAKAHASHI[2], and Nobuyuki OSHIMA[3],

Hokkaido University, Kita 13 Nishi 8, Kita-ku, Sapporo, Hokkaido 060-8628, Japan,

and

Hisashi KIHARA[4]

Kyushu University, 744 Motooka Nishi-ku, Fukuoka, Fukuoka 819-0395, Japan

Abstract

Reentry blackout phenomenon, which is the communication cut-off between the reentry vehicle and ground station, is a crucial problem that needs to be addressed. To improve safety during reentry, a new mitigation method was proposed using the surface catalysis effect. However, this method has not been investigated extensively by experimental methods. In this study, we experimentally demonstrated the mitigation method using a 1 MW arc-heated wind tunnel and numerically clarified the mitigation mechanism. As a demonstration experiment, communication tests were conducted for comparing

[1] Graduate Student, Graduate School of Engineering; thide3224@eis.hokudai.ac.jp

[2] Assistant Professor, Faculty of Engineering; ytakahashi@eng.hokudai.ac.jp

[3] Professor, Faculty of Engineering; oshima@eng.hokudai.ac.jp

[4] Assistant Professor, Faculty of Engineering; kihara@aero.kyushu-u.ac.jp

the two cases. In the first case, a ceramic surface was used as a low catalytic wall, whereas in the second case, a copper surface was used as a high catalytic wall in the arc-heated wind tunnel. The experimental results indicated that the blackout occurred when alumina was used as the low catalytic wall. On the other hand, for the high catalytic wall using copper, blackout was avoided. The tests were reproduced in the wind tunnel using a numerical simulation technique. From the simulation results, the mitigation mechanism suggested that: 1) the number of nitrogen and oxygen atoms decreased due to catalysis; 2) forward reactions of electron impact ionization were suppressed due to the decrease in the number of atoms; and 3) the suppression of reactions decreased the number of electrons, thereby mitigating the reentry blackout. Additionally, the numerical simulations performed on the reentry plasma around the reentry capsule suggested that the mitigation mechanisms between the arc-heated wind flow and reentry plasma were similar despite the different airflow conditions.

Keywords: Arc-heated wind tunnel; Plasma flow; Atmospheric reentry; Blackout mitigation

Nomenclature

e = Elementary charge, $\mathrm{C} = \mathrm{s} \cdot \mathrm{A}$

f = frequency, $\mathrm{Hz} = \mathrm{s}^{-1}$

m = Mass, kg

n = Number density, m^{-3}

γ = Catalytic recombination coefficient

ε_0 = Permittivity in free space, $\mathrm{Fm^{-1}} = \mathrm{m^{-3}kg^{-1}s^4A^2}$

ρ = density, $\mathrm{kg\,m^{-3}}$

$\dot{w}$ = mass production rate, $\mathrm{kg\,m^{-3}s^{-1}}$

$\dot{N}$ = production rate, $\mathrm{m^{-3}s^{-1}}$

Subscripts

e = Electron

s = Species

w = Wall

1 Introduction

The reentry blackout phenomenon is a common problem encountered during atmospheric reentry, wherein the communication between the reentry vehicle and ground station is cut off. Atmospheric reentry is a critical and inevitable stage while returning from space. During reentry, plasma is generated near the reentry vehicle due to the dissociation and ionization of gases by the strong shock wave. This high-density plasma attenuates and reflects the electromagnetic waves used for telecommunication, thereby causing a reentry blackout.

Hence, it is desirable to devise a mitigation method to avoid or mitigate the reentry blackout. By mitigating reentry blackout, it is possible to continue receiving the location information of the vehicle during reentry. Additionally, this information improves the accuracy of landing point prediction,

which reduces recovery costs after landing.

To mitigate reentry blackout, it is important to reduce the electron number density near the reentry vehicle. As the ions and electrons are drifting in the reentry plasma, positive or negative space charges appear locally. As a result, ions attract electrons via the Coulomb force and form a simple harmonic motion. The frequency f_{p} of this oscillation is called the plasma frequency, which is expressed by Eq. (1).

$$f_{\mathrm{p}} = \frac{1}{2\pi}\sqrt{\frac{\mathrm{e}^2 n_{\mathrm{e}}}{\mathrm{m_e}\varepsilon_0}} \tag{1}$$

where e, n_e, ε_0, and m_e are the elementary charge, electron number density, permittivity in free space, and mass of electron, respectively. The plasma frequency is a function of the electron number density. Reentry blackout generally occurs when the plasma frequency f_{p} exceeds the frequency of the electromagnetic wave f_{link} used for communication, i.e., $f_{\mathrm{p}} \geq f_{\mathrm{link}}$. When the frequency of the electromagnetic wave f_{link} is 2.4 GHz, the critical electron number density $n_{\mathrm{e,crit}}$ at which the reentry blackout occurs is calculated using Eq. (2).

$$n_{\mathrm{e,crit}} = 4\pi^2\varepsilon_0 \mathrm{m_e} f_{\mathrm{link}}^2/\mathrm{e}^2 = 7.137 \times 10^{16}\ \mathrm{m}^{-3} \tag{2}$$

Various methods, such as the use of lasers [1], magnetic windows [2,3], and injection of liquid electrophilic substances [4,5], have been proposed for mitigating reentry blackout. The injection of liquid electrophilic substances into the fluid reduces the plasma density. Belov et al. [6] investigated an aerodynamic shaping technique by placing communication antennas in special small containers in front of a blunt-nosed vehicle. Kim et al. [7] reported an electromagnetic $\boldsymbol{E} \times \boldsymbol{B}$ layer approach for

mitigating reentry blackout. By applying the $\boldsymbol{E} \times \boldsymbol{B}$ layer around the antenna, a plasma window is formed so that electromagnetic waves can pass through the plasma. Takahashi et al. [8] suggested that an inflatable reentry vehicle can reduce plasma. Deceleration at high altitudes, which occurs due to the large area and low mass of the inflatable vehicle, decreases the free-stream density, which reduces the number of electrons generated by the shock wave.

Jung et al. [9] and Takahashi et al. [10] performed a numerical analysis considering the catalytic recombination reaction for a reentry vehicle using the atmospheric reentry demonstrator (ARD). The surface material of the reentry vehicle functions as a catalyst. Therefore, the dissociated and ionized gas atoms and electrons recombine when they collide on the wall and leave. Furthermore, it was confirmed that surface catalysis reduces the electron number density in the wake behind the vehicle. This indicated the effect of mitigating reentry blackout numerically.

However, the mitigation method has not been demonstrated experimentally. Thus, it is necessary to experimentally test reentry blackout mitigation via surface catalysis effects. We propose the use of an arc-heated wind tunnel. An arc-heated wind tunnel is a facility used to generate high-temperature plasma that can simulate the reentry environment.

The objectives of this study are to demonstrate the mitigation method of reentry blackout via catalytic recombination and analyze this mitigation mechanism via numerical analysis. Recently, airflow identification in arc-heated wind tunnels has demonstrated the distribution of various quantities [11,12], including translational temperature, enthalpy, and Mach number. We expect that these results

will accelerate the mitigation study of reentry blackouts in wind tunnel experiments. In this study, we reproduced the reentry environment using a 1 MW arc-heated wind tunnel at the Institute of Space and Astronautical Science (ISAS) of the Japan Aerospace Exploration Agency (JAXA). In this experiment, a test model containing a communication module was placed in the arc-heated flow to perform a communication test. In the numerical analysis, plasma flow analysis in the ISAS 1 MW arc-heated wind tunnel was performed. In addition, the mitigation mechanism around the atmospheric reentry demonstrator (ARD) [13] was investigated. The numerical analysis for the re-entry of ARD was based on the results obtained by Takahashi et al. [10].

2 Communication Test

2.1 Experimental setup

This communication test was conducted to demonstrate the mitigation of reentry blackout via surface catalytic recombination. The ISAS 1 MW arc-heated wind tunnel [14], which has a segmented type arc heater consisting of an anode chamber, cathode chamber, constrictor section, throat section, and nozzle section, was used as the test device. The exit diameter of the nozzle was 25 mm, whereas the mass flow rates of the test gas were between 10 and 30 g/s. The discharge current could be varied between 300 and 700 A, and the maximum input power of the arc heater was approximately 1 MW. The flow enthalpy ranged from 3 – 20 MJ/kg, and the impact pressure at the test chamber was 5 – 70 kPa. The ISAS arc-heated wind tunnel is shown in Figure 1, whereas the operating conditions are listed in Table 1.

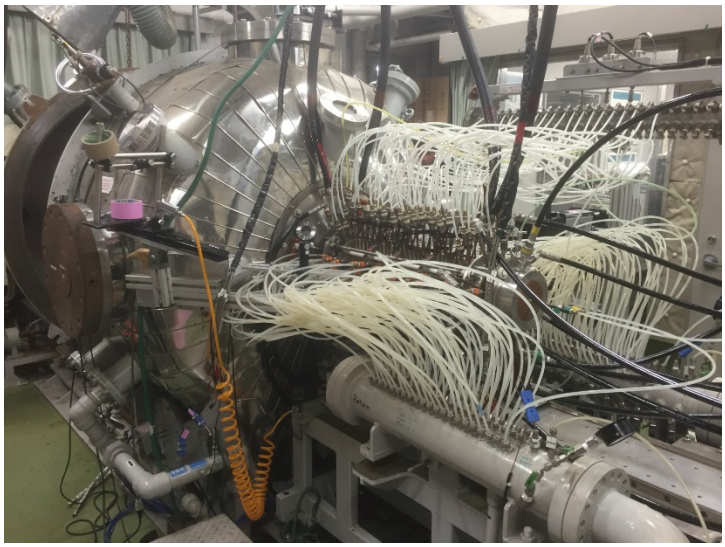


Figure 1. ISAS 1 MW arc-heated wind tunnel.

Table 1. Operating conditions of the 1 MW arc-heated wind tunnel.

Test gas	Air
Mass flow rate, g/s	18
Total temperature of inlet gas, K	300
Input current, A	450

Figure 2 shows a picture of the test models containing the communication module. The test model had an 80 mm long cylindrical shape with a 50 mm diameter. Alumina and copper were used as the low catalytic material [15] and high catalytic material [16], respectively, to confirm the difference between the catalytic recombination reactions. As shown in Figure 2, only the front material of the model was different. The side materials of both the models were copper. During the experiment, the

communication modules were covered with ceramic and thermal insulation materials. The ceramic material was used to protect the communication module from radiation. TWELITE 2525A (TWE-L-2525A, Mono Wireless Inc., Japan) and MONOSTICK (MONOSTICK-C, Mono Wireless Inc., Japan) were used as the transmitter and receiver, respectively. The frequency of these communication devices was 2.4 GHz. In the ARD, a 2.25 GHz communication equipment was used for communication with the tracking and data relay satellites. TWELITE 2525A and MONOSTICK were selected because these devices were easy to obtain and their frequency relatively close to that of ARD.

In this study, a high catalytic material refers to a material with a relatively high catalytic recombination coefficient γ. The catalytic recombination coefficient indicates the ratio at which the dissociated and ionized gas atoms and electrons recombine when they collide with the wall and are eliminated. At $\gamma = 0$, a non-catalytic wall condition exists, i.e., no catalytic recombination reaction occurs. At $\gamma = 1$, a finite catalytic wall condition exists, where all atoms colliding on the wall surface recombine. Table 2 shows the examples of catalytic recombination coefficients.

Table 2. Examples of catalytic recombination coefficient [15,16].

Atomic species/Wall material	γ_s	T_w, K

O/AL_2O_3	0.029~0.051	1000
O/Cu	0.1	950
N/Cu	0.37	950

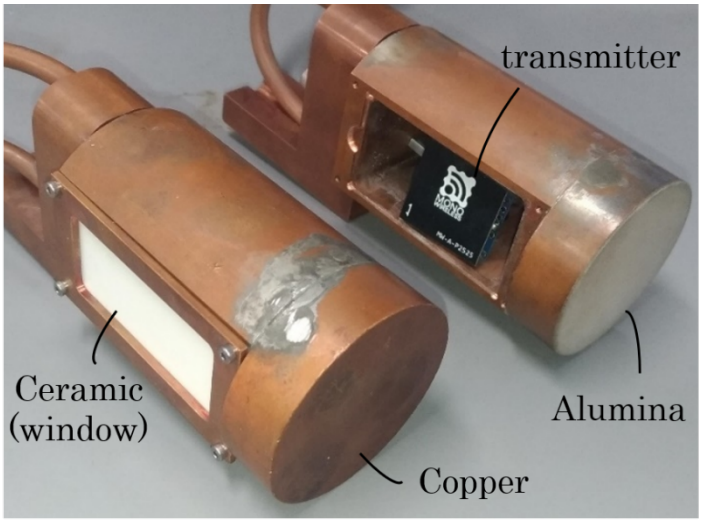


Figure 2. Test model containing the communication module.

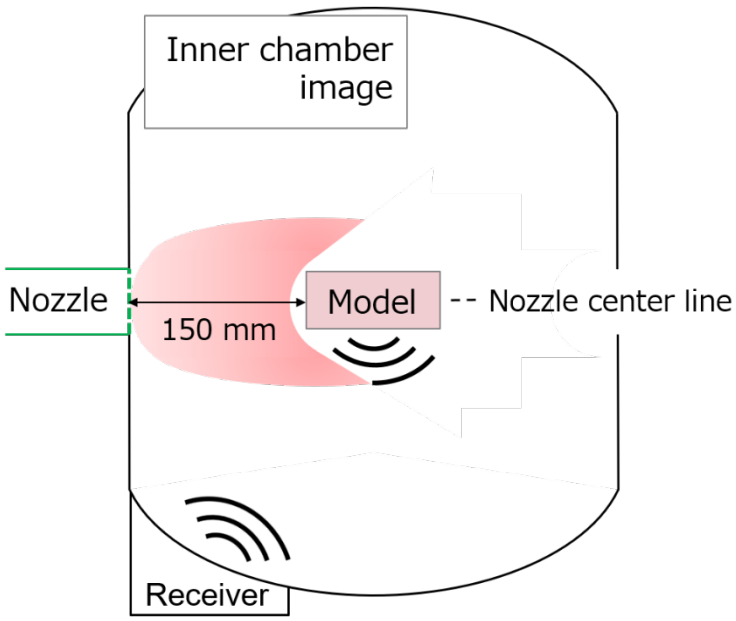


Figure 3. Inner chamber image.

Figure 3 shows the inner chamber. The receiver was fixed outside the test chamber of the arc-heated wind tunnel. The model was first kept outside the plasma flow and then placed inside the flow at 150 mm from the nozzle exit on the nozzle center line. After exposure to the plasma flow for 2 s, the model was retracted to the standby position. The communication power of the receivers was recorded before plasma exposure until it returned to the initial position.

3 Numerical Method

The experimental conditions were reproduced numerically, where the test model containing the communication module was installed in the chamber of a 1 MW arc-heated wind tunnel [14].

3.1 Plasma Flow

It was assumed that the plasma flow in the arc-heated flow was laminar, steady, and continuum. Additionally, the present simulation model accounts for the possibility of thermochemical nonequilibrium. To express thermal nonequilibrium, Park's two-temperature model, which separates the temperature into translation-rotation and vibration-electron temperatures, was adopted.

The governing equations of the flow field were composed of total mass, momentum, total energy, species mass, and vibration-electron energy conservation in addition to the equation of state. For modeling the chemical nonequilibrium in high-temperature air, the gas was assumed to consist of 11 chemical species ($N_2, O_2, NO, N_2^+, O_2^+, NO^+, N, O, N^+, O^+$, and e^-), and 49 reactions that were assumed to occur are listed in Table 3. The equilibrium constants for the 49 chemical reactions were

calculated using the curve-fit formula given by the Park's model [17] and Gupta's model [18].

Table 3. Chemical reactions [19].

reaction no	Forward		Backward
1 – 6	$N_2 + M_1$	$\rightleftharpoons$	$N + N + M_1$
7 – 10	$N_2 + M_2$	$\rightleftharpoons$	$N + N + M_2$
11	$N_2 + e^-$	$\rightleftharpoons$	$N + N + e^-$
12 – 17	$O_2 + M_1$	$\rightleftharpoons$	$O + O + M_1$
18 – 21	$O_2 + M_2$	$\rightleftharpoons$	$O + O + M_2$
22 – 27	$NO + M_1$	$\rightleftharpoons$	$N + O + M_1$
28 – 31	$NO + M_2$	$\rightleftharpoons$	$N + O + M_2$
32	$NO + O$	$\rightleftharpoons$	$N + O_2$
33	$N_2 + O$	$\rightleftharpoons$	$NO + N$
34	$N + N$	$\rightleftharpoons$	$N_2^+ + e^-$
35	$O + O$	$\rightleftharpoons$	$O_2^+ + e^-$
36	$N + O$	$\rightleftharpoons$	$NO^+ + e^-$
37	$N + e^-$	$\rightleftharpoons$	$N^+ + e^- + e^-$
38	$O + e^-$	$\rightleftharpoons$	$O^+ + e^- + e^-$
39	$NO^+ + O$	$\rightleftharpoons$	$N^+ + O_2$

40	$O_2^+ + N$	$\rightleftharpoons$	$N^+ + O_2$
41	$O^+ + NO$	$\rightleftharpoons$	$N^+ + O_2$
42	$O_2^+ + N_2$	$\rightleftharpoons$	$N_2^+ + O_2$
43	$O_2^+ + O$	$\rightleftharpoons$	$O^+ + O_2$
44	$NO^+ + N$	$\rightleftharpoons$	$O^+ + N_2$
45	$NO^+ + O_2$	$\rightleftharpoons$	$O_2^+ + NO$
46	$NO^+ + O$	$\rightleftharpoons$	$O_2^+ + N$
47	$O^+ + N_2$	$\rightleftharpoons$	$N_2^+ + O$
48	$NO^+ + N$	$\rightleftharpoons$	$N_2^+ + O$
49	$N_2 + N^+$	$\rightleftharpoons$	$N_2^+ + N$

$M_1 = N_2, O_2, NO, N_2^+, O_2^+, NO^+$

$M_2 = N, O, N^+, O^+$

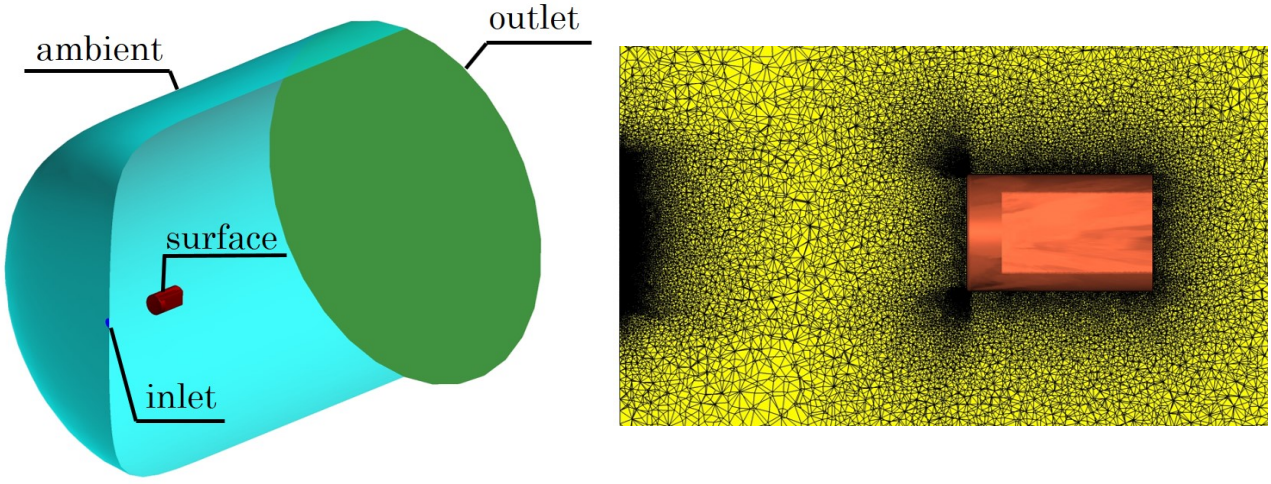
The mass production rates of all chemical species were calculated using the forward and backward reaction rates. The forward reaction rate coefficients were obtained from Park's work [19][1], whereas the backward reaction rate was evaluated using the corresponding equilibrium constant [17,18].

The governing equations of plasma flow, including the aforementioned physical models, were solved using a cell-centered finite volume approach. Evaluation of the advection fluxes across the cell interface in the equations was performed using the simple low-dissipation AUSM (SLAU) scheme

[20]. Furthermore, the viscous fluxes were calculated by the average value between the gradients of neighboring computational cells. The weighted Green–Gauss method was adopted for calculating the spatial gradients of the flow properties. Moreover, time integration was performed using an implicit time-marching approach. The matrix solver of the governing equation system was the lower-upper symmetric Gauss–Seidel method coupled with the point-implicit method [21] for stable computation of the source term.

The numerical models were implemented on a high-enthalpy flow solver RG-FaSTAR [22]. This software, which is a version of the fast unstructured CFD code FaSTAR [23], incorporates real gas effects and thermochemical nonequilibrium, and was developed by JAXA. For massive parallel computations on a high-performance computer, the message passing interface technique with a domain partition approach was introduced. The computations were performed on the ITO computer system of the Research Institute for Information Technology, Kyushu University.

3.2 Calculation Conditions



(a) Boundary conditions (b) Computational grids

Figure 4. Computational domain for plasma flow simulation.

Figure 4 shows the computational domain for the present plasma flow simulation. The majority of the computational grids in the computational domain were composed of tetrahedral meshes. However, triangular prism meshes were laminated near the test model surface and inflow boundaries. The total number of computational cells was approximately 27 million.

Figure 5 shows the flow enthalpy of radial distribution at the nozzle exit. This was determined based on the results computed by Takahashi et al. [11]. The operating conditions of the wind tunnel test are air flow, 450 A of input current, and 18 g/s of input mass flow rate. For these operating conditions, the inlet parameters at the nozzle exit exhibited this distribution.

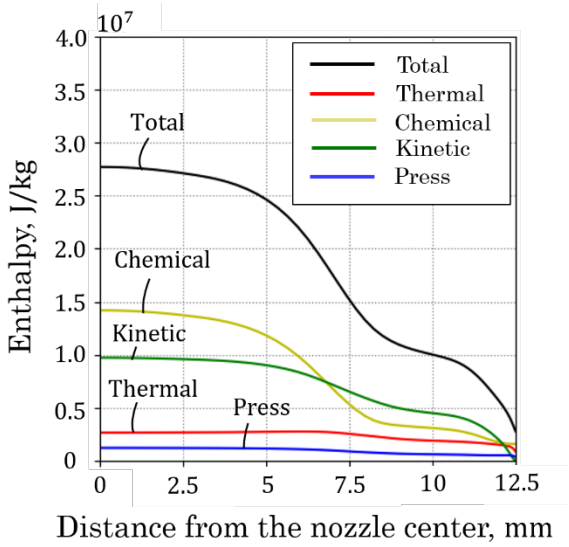


Figure 5. Radial profiles of flow enthalpy at the nozzle exit of 1 MW arc heater.

The temperature and pressure were fixed at ambient conditions and a gradient-free condition for all flow variables was imposed at the outflow. At the surface boundary, a non-slip condition for velocity

and no pressure gradient condition normal to the surface were imposed. The surface temperature T_w was fixed at 300 K, which is closer to the experimental conditions. Note that the effects of the wall temperature on the catalysis recombination coefficient are small. The test model containing the communication module had a cylindrical shape having a diameter of 50 mm and length of 80 mm and is the same shape as in the experiment. This model was located 150 mm downstream from the nozzle exit on the center line.

The surface catalysis, i.e., the finite catalytic condition, is described in Eq. (3) [24].

$$\rho D_s \frac{dC_s}{dn} = \gamma \rho_s \sqrt{\frac{R_s T_w}{2\pi}} \tag{3}$$

where ρ, ρ_s, D_s, C_s, R_s, and n represent the total density, density of species, effective diffusion coefficient of species, mass fraction, gas constant of species, and coordinate along the direction normal to the wall surface, respectively. The left hand side of Eq. (3) represents the mass flux of atoms by diffusion (given by Fick's first law), whereas the right hand side represents the mass of chemical species that collide on the surface (determined by gas molecular kinetics). We considered the following two catalysis reactions:

$$\mathrm{N} + \mathrm{N} + (\mathrm{surface}) \rightarrow \mathrm{N_2} + (\mathrm{surface}) \tag{R1}$$

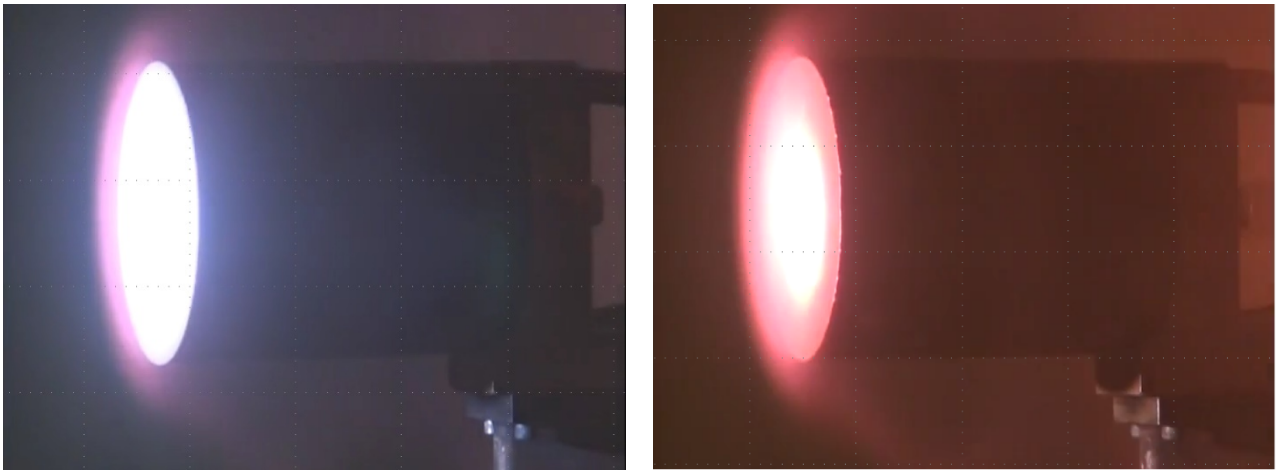
$$\mathrm{O} + \mathrm{O} + (\mathrm{surface}) \rightarrow \mathrm{O_2} + (\mathrm{surface}) \tag{R2}$$

The analysis was performed on two cases, i.e., when all the faces of the model were $\gamma = 0$, and when the same region was $\gamma = 1$.

4 Results and Discussion

4.1 Experimental Results

Figure 6 shows photographs of the plasma in front of the test models taken during the experiment. These images suggest that a shock wave was generated in front of the model. Additionally, it was confirmed that the high-temperature gas formed in the shock layer emitted light.



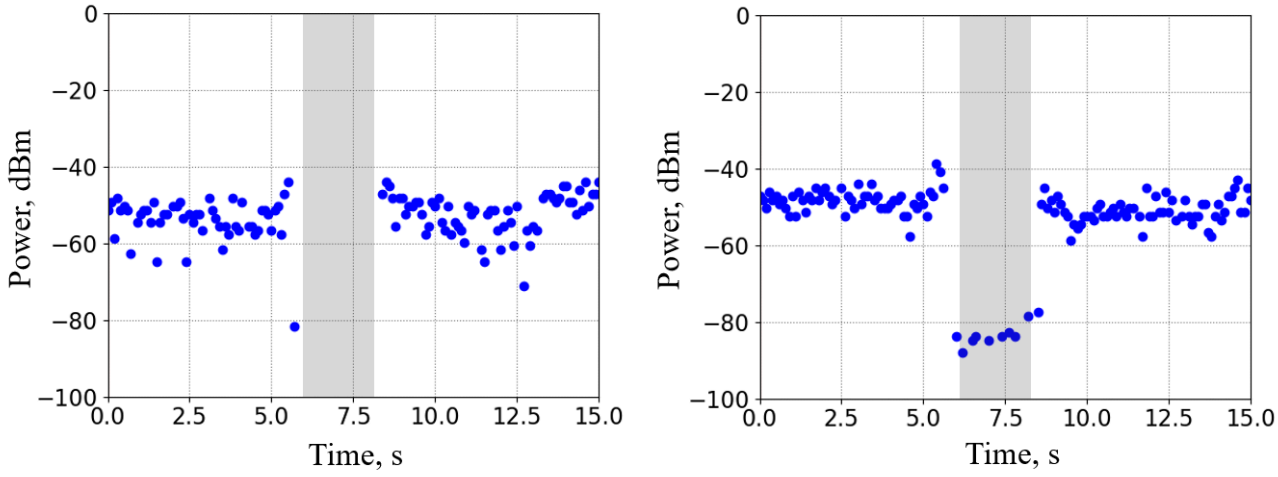
(a) Low catalytic material (Ceramic). (b) High catalytic material (Copper).

Figure 6. Image of the plasma taken during the experiment.

Figure 7 compares the measurement results of the power for the alumina and copper models. The model started to move from the standby position after approximately 5 s, and arrived at the plasma flow input position after approximately 0.5 s. The gray areas in the figure show the time when the model stopped in the plasma for 2 s.

For the low-catalytic wall using alumina, the communication was maintained although it was disrupted when the model was exposed to the plasma flow. Nevertheless, the communication was recovered while leaving the flow. This indicates that reentry blackout occurs in the plasma flow for the

low-catalysis case. On the other hand, for the high-catalytic wall using copper, the communication was maintained even when the model was injected into the plasma although attenuation of electromagnetic waves was observed. These results suggested that the experimental demonstration for mitigating reentry blackout via the catalytic effect was performed.



(a) Low catalytic material (Ceramic). (b) High catalytic material (Copper).

Figure 7. Communication power history (minimum detection level: -100 dBm).

4.2 Computed Distributions of Plasma Flows

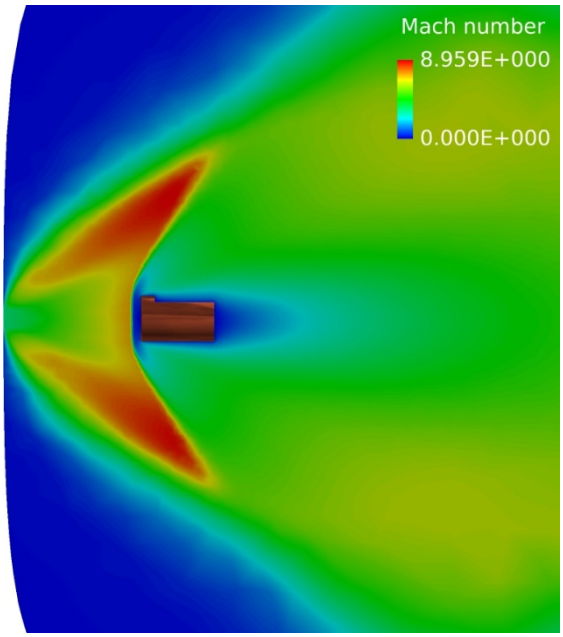


Figure 8. Distribution of Mach number.

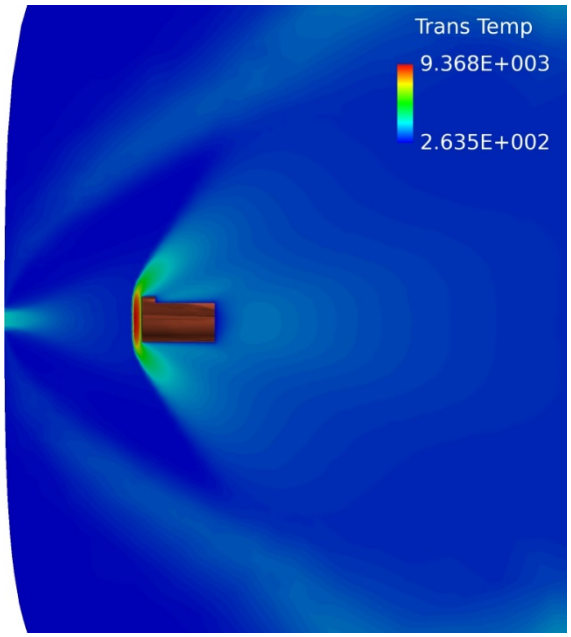
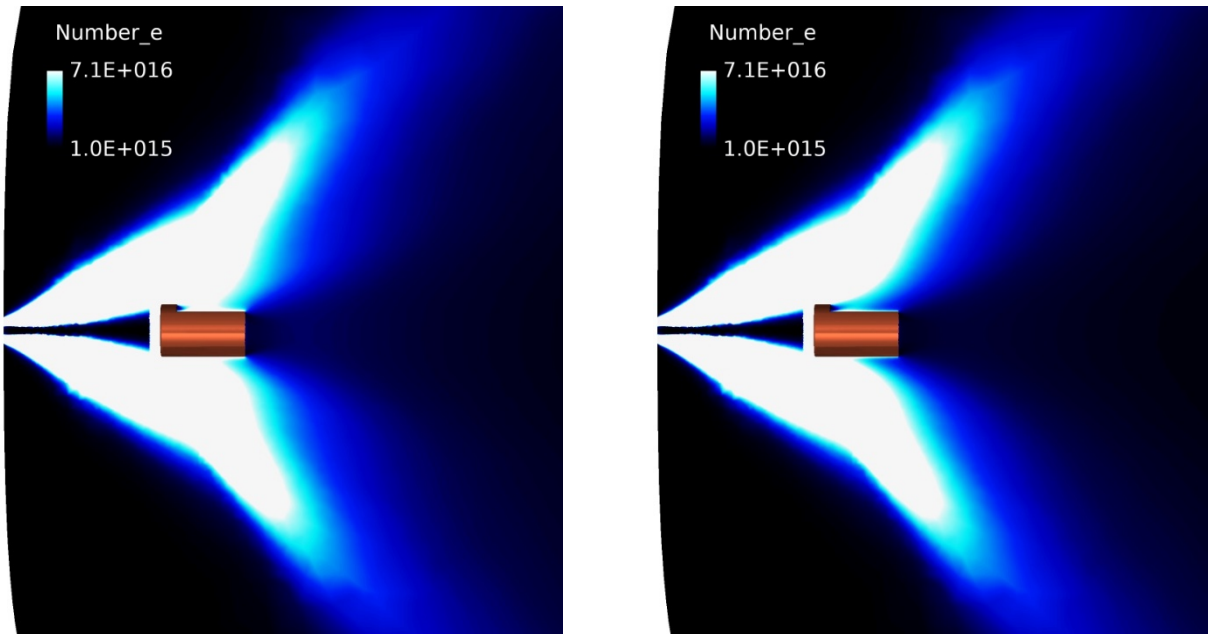


Figure 9. Distribution of translation temperature, K.

Figure 8 and Figure 9 show the distributions of the Mach number and translation temperature on the cross section of the test model, respectively. It was confirmed from the Mach number that a strong shock wave was generated in front of the model. Additionally, there were regions where the Mach number increased at the top and bottom areas of the model. This was caused by the expansion of the gas with inflow toward the low-pressure region in the test chamber. It was observed that the Mach number decreases across the shock wave. Furthermore, the distributions of the translation temperature confirmed that the temperature increased behind the shock wave in front of the model.



(a) Non-catalytic wall ($\gamma = 0$). (b) Finite-catalytic wall ($\gamma = 1$).

Figure 10. Distribution of electron number density, $1/\,\mathrm{m}^3$.

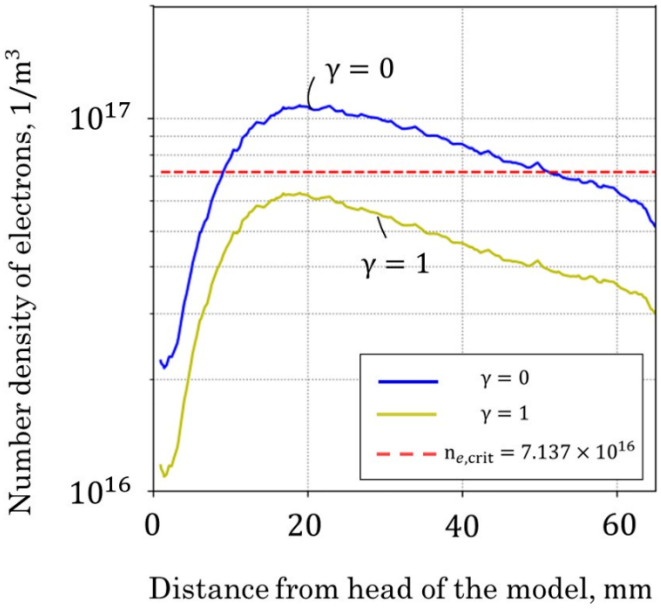


Figure 11. Electron number density profile at 2 mm above the window.

Figure 10 shows the distributions of electron number density for non-catalytic $(\gamma = 0)$ and

finite-catalytic walls ($\gamma = 1$). The upper limit value of the legends in the figure is the critical electron number density $n_{e,crit}$: $7.137 \times 10^{16}\ \mathrm{m}^{-3}$. The dissipation of electromagnetic waves used for telecommunication occurs in the white regions shown in Figure 10. Figure 11 shows the electron number density profile at 2 mm above the window; the electron number densities on the surface are not presented. The surface boundary condition for the electron conservation equation does not potentially reproduce the electron density behavior because of the relatively simple modeling. In the simulations, the surface temperature of the model was set to 300 K, which could overpredict the total density and electron number density near the surface. From Figure 11, it was confirmed that the electron number density near the model surface for the finite-catalytic wall decreases to the level at which the reentry blackout does not occur.

4.3 Mitigation Mechanism

Since the reentry blackout depends on the electron number density, we focused on the reactions that produced electrons to elucidate the mitigation mechanism. Reactions R3 to R7 were responsible for producing electrons in the present simulation model. R3 to R5 represent associative ionization reactions, whereas R6 and R7 are electron impact ionization reactions.

$$\mathrm{N} + \mathrm{N} \rightleftharpoons \mathrm{N}_2^+ + \mathrm{e}^- \quad \text{(R3)}$$

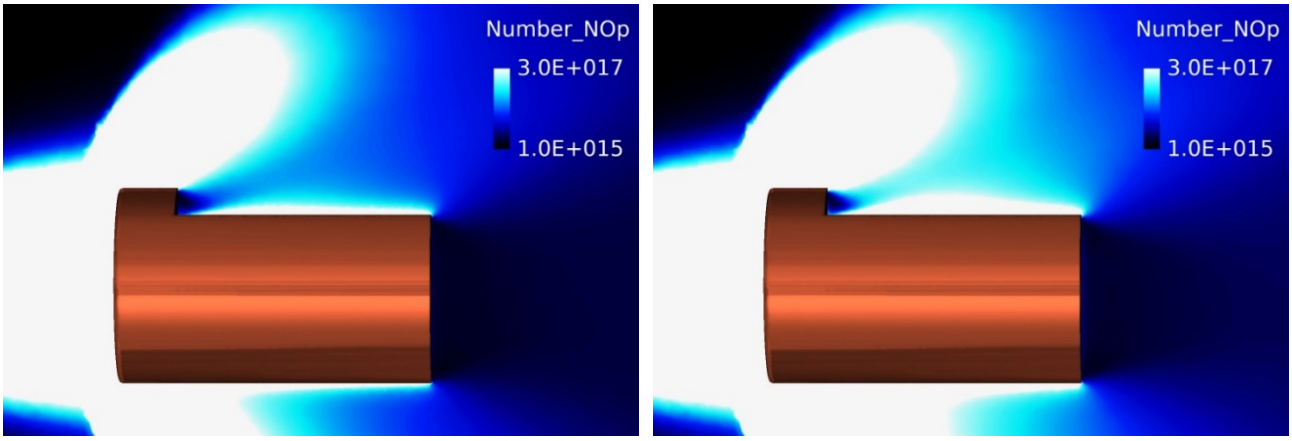
$$\mathrm{O} + \mathrm{O} \rightleftharpoons \mathrm{O}_2^+ + \mathrm{e}^- \quad \text{(R4)}$$

$$\mathrm{N} + \mathrm{O} \rightleftharpoons \mathrm{NO}^+ + \mathrm{e}^- \quad \text{(R5)}$$

$$N + e^- \rightleftharpoons N^+ + e^- + e^- \quad \text{(R6)}$$

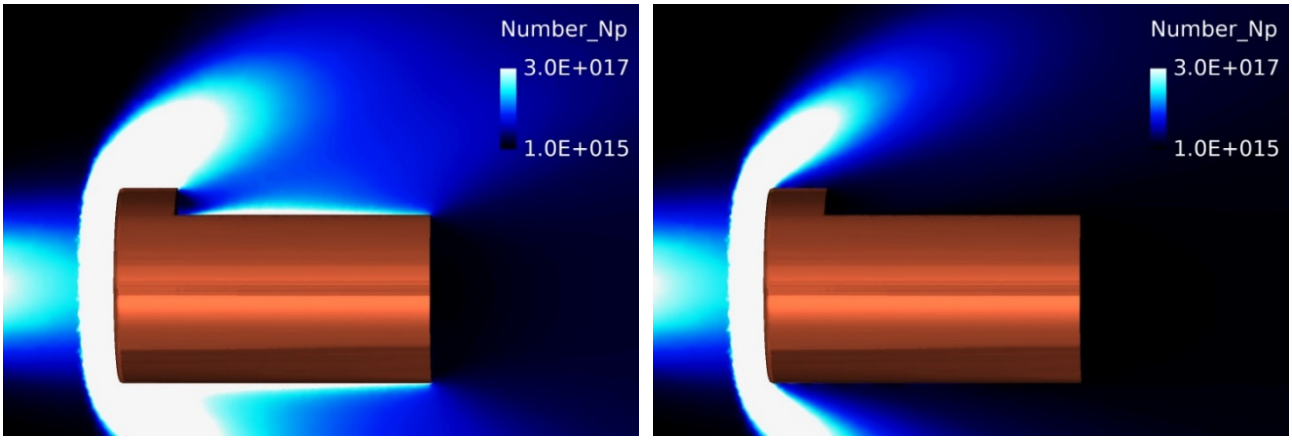
$$O + e^- \rightleftharpoons O^+ + e^- + e^- \quad \text{(R7)}$$

Figure 12 and Figure 13 show the respective number density distributions of NO^+ and N^+ used in associative ionization and electron impact ionization. For visualizing the difference between the increase and decrease in the number density of ion species that appeared in these two ionizations, we indicated the number densities of NO^+ and N^+ as representative species. A large number of NO^+ already appeared in the arc-heated flow, which was in front of the shock wave, as shown in Figure 12. It was confirmed in a previous study [11] that NO^+ existed at the nozzle of the 1 MW arc heater. Conversely, N^+ was mainly produced across the shock wave, as shown in Figure 13. Since the number density of NO^+ was roughly equal to that of N^+ in the case of a non-catalytic wall near the window surface, both associative ionization and electron impact ionization affected the reentry blackout in the arc-heated wind tunnel.



(a) Non-catalytic wall ($\gamma = 0$). (b) Finite-catalytic wall ($\gamma = 1$).

Figure 12. Number density distribution of NO^+, $1/\,m^3$.



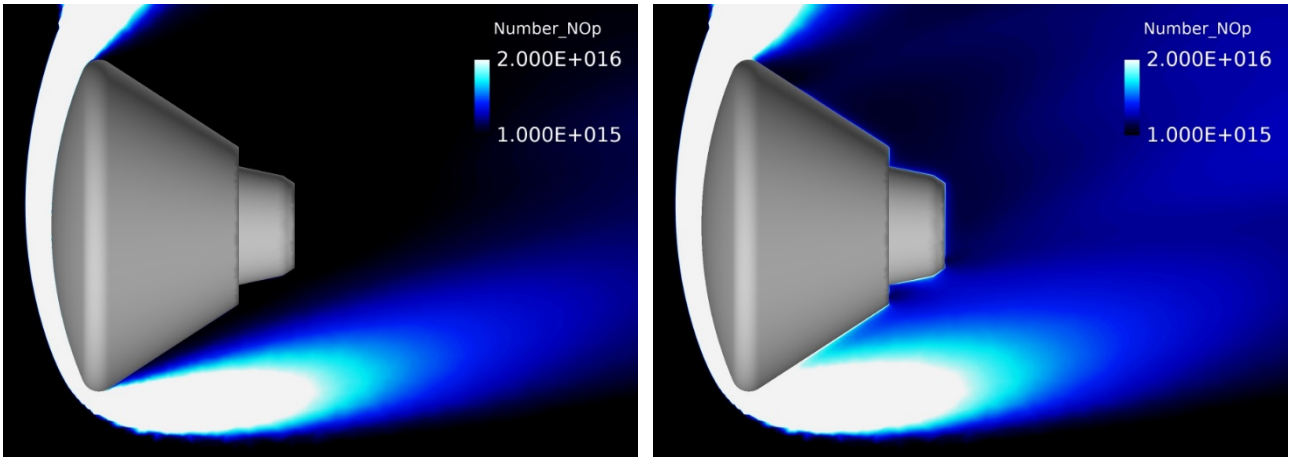
(a) Non-catalytic wall ($\gamma = 0$). (b) Finite-catalytic wall ($\gamma = 1$).

Figure 13. Number density distribution of N^+, $1/m^3$.

By comparing the number density distribution of NO^+ at the non-catalytic and finite-catalytic walls, as shown in Figure 12, the number density of NO^+ increased near the wall owing to the catalytic effect. The decrease in the number of electrons near the model inhibited the inverse reactions of associative ionization. Therefore, we found that inverse associative ionization did not contribute to the mitigation of reentry blackouts. Conversely, as shown in Figure 13, a comparison of the number density distribution of N^+ for the non-catalytic and finite-catalytic walls cases indicated that the N^+ number density decreased near the wall due to the catalytic effect. This means that the forward reactions of electron impact ionization were suppressed, thereby mitigating reentry blackouts. These reactions are likely to occur as follows: 1) the number of nitrogen and oxygen atoms decreases due to catalytic recombination reactions R1 and R2, and 2) the forward reactions of electron impact ionization were suppressed due to the decrease in the number of atoms.

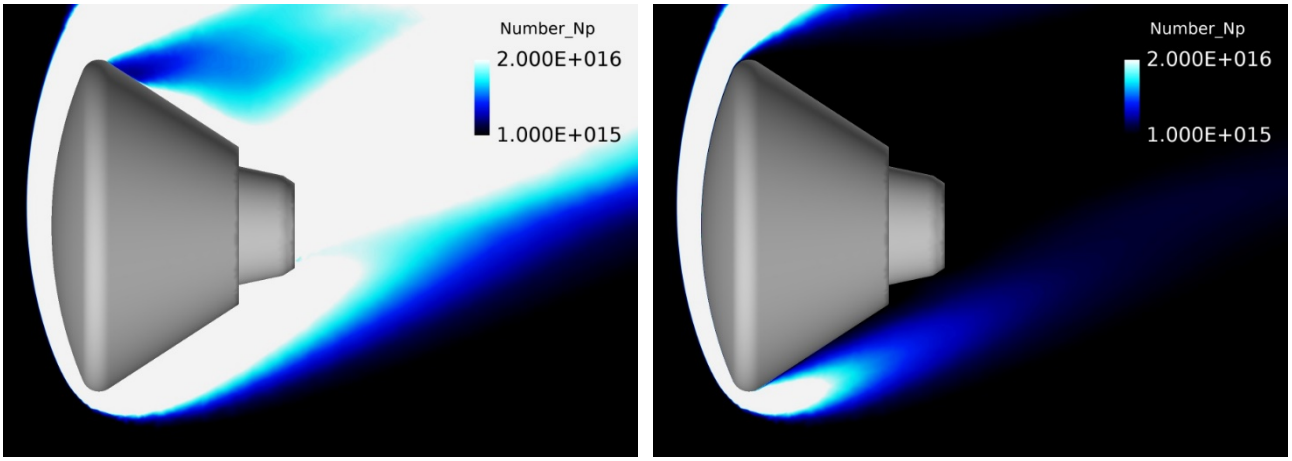
4.4 Electron Reduction in Atmospheric Reentry

We investigated the mitigation mechanism during reentry because the results in the arc-heated wind tunnel can be applied to the reentry vehicle if the mitigation mechanism of reentry is similar to that of the arc-heated wind tunnel.



(a) Non-catalytic wall ($\gamma = 0$). (b) Finite-catalytic wall ($\gamma = 1$).

Figure 14. Number density distribution of NO^+, $1/\,m^3$.



(a) Non-catalytic wall ($\gamma = 0$). (b) Finite-catalytic wall ($\gamma = 1$).

Figure 15. Number density distribution of N^+, $1/\,m^3$.

Figure 14 and Figure 15 show the respective number density distributions of NO^+ and N^+ for associative ionization and electron impact ionization around ARD at an altitude of 85 km. The number densities were calculated based on the computed results obtained by Takahashi et al. [10]. Since a large number of N^+ were generated near the ARD, the electron-impact ionization reaction was the dominant reaction that resulted in reentry blackout during reentry. Similar to the results of the arc-heated wind tunnel, the number density of NO^+ increased and that of N^+ decreased near the ARD surface. Since the tendency of chemical reactions in the arc-heated wind tunnel and reentry are similar, the mitigation mechanism of the reentry blackout is similar to that of the arc-heated wind tunnel. In other words, we found that the number of electrons decreased due to the suppression of the electron impact ionization reaction. This reaction was suppressed due to an increase in the number of nitrogen and oxygen atoms, which was caused by the catalytic effect.

5 Conclusions

In this study, an experimental test was performed in the 1 MW arc-heated wind tunnel at ISAS to demonstrate a method for mitigating reentry blackout via catalytic recombination. Furthermore, plasma flow analyses were conducted in the JAXA/ISAS 1 MW arc-heated wind tunnel and around the ARD to elucidate the mechanism of mitigating reentry blackout by catalytic effects.

The communication tests were conducted by using copper as the high catalytic material and

alumina as the low catalytic material. However, a reentry blackout occurred only in the case of the low-catalytic wall, whereas the communication was not blocked by the plasma for the high-catalytic wall. These results suggested that experimental demonstration for mitigating reentry blackout via the catalytic effect was performed in this study.

The results of the numerical analysis confirmed that the electron number density near the test model decreased due to the catalytic effects. Additionally, the mitigation mechanism was described as follows: 1) the number of nitrogen and oxygen atoms decreased because of the catalysis; 2) the forward reactions of electron impact ionization were suppressed due to the decrease in the number of atoms; and 3) the suppression of reactions decreased the number of electrons, thereby mitigating the reentry blackout. Furthermore, it was found that these mechanisms were common even though there was a difference in airflow conditions between the arc-heated wind tunnel and atmospheric reentry.

As the catalytic reactions are heat dissipation reactions, the heat flux from the flow field to the vehicle increased. Therefore, this heat flux must be considered while designing the reentry vehicle. Moreover, only two catalytic recombination reactions in which nitrogen and oxygen molecules were generated were considered. For quantitative evaluation of the catalytic effect, it is necessary to apply the recombination reaction that generates NO. In this study, the surface catalysis effects were experimentally analyzed in an arc-heated wind tunnel. However, a real flight demonstration was not performed. In the arc-heated wind tunnel, the pressure and heat flux at the stagnation point match the reentry situation. In other words, there are differences in the distributions of velocity and chemical

species. In reentry flights, electron impact ionization is a major factor in reentry blackouts. Conversely, in the arc wind tunnel, associative ionization is another reaction that affects the electron distribution. The mitigation mechanism of the reentry blackout suppresses electron impact ionization, and the catalytic effect is expected to be stronger during reentry flight. In addition, it is difficult to make a quantitative comparison using the communication devices used in this experiment. To confirm the effects of mitigation reentry blackouts, real flight test must be conducted in future studies.

Acknowledgments

This work was supported by JSPS KAKENHI (grant number 17KK0123). The present computational results were obtained using a fast unstructured CFD code “FaSTAR,” which was developed by JAXA. This research used the computational resources of the ITO computer provided by the Kyushu University through the HPCI System Research project (Project ID: hp190033). The present wind tunnel experiments were conducted at the arc wind tunnel facility provided by the Institute of Space and Astronautical Science, Japan Aerospace Exploration Agency as an inter-university research institute facility (Project ID: W17-04). The authors declare that they have no known competing financial interests or personal relationships that could have influenced the work reported in this paper.

References

[1] Rybak J P and Churchill R J 1971 Progress in Reentry Communications *IEEE Transactions on Aerospace and Electronic Systems* **7** 879–894 doi:10.1109/TAES.1971.310328

[2] Hodara H 1961 The Use of Magnetic Fields in the Elimination of the Re-Entry Radio Blackout *Proceedings of the IRE* **49** 1825–1830 doi:10.1109/JRPROC.1961.287709

[3] Bendoukha S A, Okuyama K, Szasz B and Ward T 2017 A Study of Radio Frequency Blackout for Space Probe During Atmospheric Reentry Phase *International Journal of Research - GRANTHAALAYAH* **5** 1–15 doi:10.5281/zenodo.439549

[4] Good R and Rossi J J 1966 An Injection System for Alleviation of Radio Blackout During Re-Entry *MITHRAS CAMBRIDGE MA* No. MC-63-78-R2

[5] Schroeder L C and Russo F P 1968 Flight Investigation and Analysis of Alleviation of Communications Blackout by Water Injection During Gemini 3 Reentry *Report* NASA TM X-1521 Pp 1–56

[6] Belov I F, Borovoy V Y, Gorelov V A, Kireev A Y, Korolev A S and Stepanov E A 2001 Investigation of Remote Antenna Assembly for Radio Communication with Reentry Vehicle *Journal of Spacecraft and Rockets* **38** 249–256 doi:10.2514/2.3678

[7] Kim M, Keidar M and Boyd I D 2008 Analysis of an Electromagnetic Mitigation Scheme for Reentry Telemetry Through Plasma *Journal of Spacecraft and Rockets* **45** 1223–1229 doi:10.2514/1.37395

[8] Takahashi Y, Yamada K and Abe T 2014 Examination of Radio Frequency Blackout for an Inatable Vehicle during Atmospheric Reentry *Journal of Spacecraft and Rockets* **51**(2): 430-441 doi:10.2514/1.A32539

[9] Jung M, Hisashi K, Abe K and Takahashi Y 2017 Numerical Simulation of Plasma Flows and Radio-Frequency Blackout in Atmospheric Reentry Demonstrator Mission *In 47th AIAA Fluid Dynamics Conference* p. 3308 doi:10.2514/6.2017-3308

[10] Takahashi Y, Enoki N, Takasawa H and Oshima N 2020 Surface Catalysis Effects on Mitigation of Radio Frequency Blackout in Orbital Reentry *Journal of Physics D: Applied Physics* **53** doi:10.1088/1361-6463/ab79e0

[11] Takahashi Y, Enoki N and Koike T 2020 Flow Enthalpy of Non-equilibrium Plasma in 1 MW Class Arc-Heated Wind Tunnel *AIAA Paper* **59**(1): 263-275 doi:10.2514/1.J058407

[12] Lee J Il, Kim C and Kim K H 2007 Accurate Computations of Arc-Heater Flows Using Two-Equation Turbulence Models *Journal of Thermophysics and Heat Transfer* **21** 67–76 doi:10.2514/1.25495

[13] Tran P and Paulat J 2007 Re-entry Flight Experiments Lessons Learned – The Atmospheric Reentry Demonstrator ARD *Nato RTO-EN-AVT-130-10* 10-46

[14] Yamada T and Inatani Y 2003 Arc Heating Facility and Test Technique for Planetary Entry Missions *The Institute of Space and Astronautical Science report SP* **17** p.147

[15] Balat-Pichelin M, Bedra L, Gerasimova O and Boubert P 2007 Recombination of atomic oxygen on α-Al2O3 at high temperature under air microwave-induced plasma *Chemical Physics* **340** 217–226 doi:10.1016/j.chemphys.2007.09.019

[16] Grumet A and Anderson J, The Effects of Surface Catalysis on the Hypersonic Shock

Wave/Boundary Layer Interaction *6th Joint Thermophysics and Heat Transfer Conference* doi:10.2514/6.1994-2073

[17] Park C 1990 *Nonequilibrium Hypersonic Aerothermodynamics* (New York: Wiley)

[18] Gupta R N, Yos J M, Thompson R A and Lee K P 1990 A Review of Reaction Rates and Thermodynamic and Transport Properties for an 11-Species Air Model for Chemical and Thermal Nonequilibrium Calculations to 30000 K *NASA* RP-1232

[19] Park C 1988 Assessment of a two-temperature kinetic model for dissociating and weakly ionizing nitrogen *Journal of Thermophysics and Heat Transfer* **2** 8–16

[20] Shima E and Kitamura K 2011 Parameter-Free simple Low-Dissipation AUSM-Family Scheme for All Speeds *AIAA Journal* **49** 1693–1709 doi:10.2514/1.J050905

[21] Jameson A and Yoon S 1987 Lower-Upper Implicit Schemes with Multiple Grids for the Euler Equations *AIAA Journal* **25**(7):929-935

[22] Takahashi Y 2016 Advanced Validation of CFD-FDTD Combined Method Using Highly Applicable Solver for Reentry Blackout Prediction *Journal of Physics D: Applied Physics Institute of Physics* **49** No. 1 015201 (15pp) doi:10.1088/0022-3727/49/1/015201

[23] Hashimoto A, Murakami K, Aoyama T, Hishida M, Ohno S, Sakashita M, Lahur P and Sato Y 2010 Development of fast flow solver FaSTAR *Proceedings of 42nd Fluid Dynamics Conference / Aerospace Numerical Simulation Symposium 2010 JAXA-SP-10-012* Pp.79-84 63 79–84

[24] Kubota H, Suzuki K and Watanuki T 2002 *Aerothermodynamics of space vehicles* (in Japanese *Utyuu Hikoutai No Netukitaigaku*) (Tokyo: University of Tokyo Press) 116-122